Ceramics International 46 (2020) 16088–16095

Contents lists available at ScienceDirect

Ceramics International

journal homepage: www.elsevier.com/locate/ceramint

Preparation of In-doped Y_2O_3 ceramics through a sol-gel process: Effects on the structural and electronic properties

Diego Richard[a,*], Mario Rentería[a], Artur W. Carbonari[b], Mariano Romero[c], Ricardo Faccio[c]

[a] Departamento de Física and Instituto de Física La Plata (IFLP, CONICET), Facultad de Ciencias Exactas, Universidad Nacional de La Plata, CC 67, 1900, La Plata, Argentina

[b] Instituto de Pesquisas Energéticas e Nucleares, Universidade de São Paulo, 05508-000, São Paulo, SP, Brazil

[c] Centro NanoMat/DETEMA, Facultad de Química, Universidad de la República (UdelaR), CC, 1157, Montevideo, Uruguay

ARTICLE INFO

Keywords:
Oxide materials
Impurities in semiconductors
Ceramics
Sol-gel process
Doping method
Hyperfine interactions

ABSTRACT

The Pechini-type sol-gel (PSG) process has been used for the preparation of doped oxides due to its capability to overcome most of the difficulties that frequently occur by using other producing methods. In this work we analyze the case of samples of pure and In-doped yttria (Y_2O_3) prepared by the PSG process. We experimentally characterize the synthesized samples by x-ray diffraction, micro-Raman spectroscopy, electrochemical impedance spectroscopy (EIS), and time-differential perturbed γ-γ angular correlation (PAC) spectroscopy, and we compare these results with those obtained starting from commercial oxide powders. We found that the PSG process can be used to successfully produce doped yttria in the cubic phase, with the impurities substitutionally located at the cationic sites of the structure. By the proposed PSG route, the inclusion of impurities does not affect the particle size nor the resistivity. However, when we compare the PSG samples with other samples produced from commercial powder, we found that the first have lower resistivities at grain interiors. On the other hand, PAC spectroscopy in ^{111}In(→^{111}Cd)-doped yttria allows the study of the dynamic hyperfine interactions observed by the radioactive ^{111}Cd impurity-probe, which can be used to "sense" the host electron availability near the impurities after the electron-capture decay of ^{111}In. Differences between PAC spectra for PSG samples and the commercial powder suggest that the PSG process introduces additional donor defects into the yttria electronic structure, which is consistent with the lower resistivity observed in the PSG samples by EIS spectroscopy.

1. Introduction

Yttrium oxide (yttria, Y_2O_3) is a traditional luminescent material which has been continuously studied for its potential technological applications. Nowadays, the use of pure and doped yttria is considered to enhance different properties in current technological devices [1–9].

In the last years, different sol-gel routes for producing pure and doped Y_2O_3 have been studied in detail [10–24]. The applicability of these processes is extensive, and their diversified uses in material science have been demonstrated [25,26]. Among them, the Pechini sol-gel (PSG) method uses common metal salts (nitrates, chlorides, acetates, etc.) as precursors, citric acid as chelating ligand of the metal ions, and a polyhydroxy alcohol (such as polyethylene glycol) as a cross-linking agent to form a polymeric resin on molecular level. This process seems to be versatile and practical in the preparation of doped nanopowders and ceramic thin films, because it reduces the segregation of metal ions, ensures the compositional homogeneity of the samples, and also for its low cost and low heat-treatment temperatures. Thus, the PSG method can overcome most of the disadvantages that other methods present, especially the physical ones (such as solid-state reaction, thermal diffusion, and ion implantation) [27,28]. Nevertheless, the samples obtained by the PSG process may present different characteristics and properties compared to those samples obtained from commercial powders or other methods. So, exhaustive studies are of paramount importance in order to develop a processing method that controls the sample properties and to improve the material performance for a given research field. In this sense, current investigations generally focus on the sample structure and morphology [11,15,21,23,29,30] using the most conventional experimental techniques [25].

In this work we present a comparative study that goes beyond these established techniques, to include an analysis of the electronic and hyperfine properties that emerge in doped yttria through the PSG

* Corresponding author. Centro de Tecnología de Recursos Minerales y Cerámica (CETMIC), CIC-CONICET, Camino Centenario y 506, CC 49, B1897ZCA, M. B. Gonnet, Argentina.

E-mail address: richard@fisica.unlp.edu.ar (D. Richard).

https://doi.org/10.1016/j.ceramint.2020.03.161
Received 26 January 2020; Received in revised form 11 March 2020; Accepted 15 March 2020
Available online 16 March 2020

process, and we compare these properties to those of samples produced from commercial powders. To this purpose, we consider a characterization that involves the use of the electrochemical impedance spectroscopy (EIS) and the time-differential perturbed γ-γ angular correlation (PAC) spectroscopy, in addition to x-ray diffraction (XRD) and micro-Raman spectroscopy. In particular, the PAC spectroscopy allows the determination of the electric field gradient (EFG) tensor at a radioactive probe-nucleus, a quantity which is highly sensitive to small changes in the electronic charge density close to that nucleus, which is usually an extremely diluted impurity in the system under study. For this reason, the EFG can be used as a powerful tool to investigate structural and electronic properties locally [31,32]. In a recent paper [21], it has been shown that the PSG method can be used to produce yttria doped with the PAC probe ^{181}Ta, doping the samples with the radioactive parent nucleus ^{181}Hf(→^{181}Ta). In that case, the hyperfine interactions in the PAC spectra reflected that the impurities occupy the two cationic sites of the cubic Y_2O_3 host structure (the *bixbyite* structure). In the present study we will extend these findings to the case of In impurities, using the PSG process to introduce the PAC probe (^{111}In→)^{111}Cd into the yttria host structure. Unlike the case of ^{181}Ta-doped yttria, for the ^{111}Cd probe nucleus it is expected the presence of time-dependent (dynamic) hyperfine interactions after the electron-capture decay of ^{111}In [31,33]. The observation of these type of time-dependent interactions is linked to the electron availability and mobility close to the probe nucleus, and depend on defects and temperature [34]. In particular, they are suited to sense charge mobility in low conductive materials, far below the detection limit of other experimental techniques [35]. So, we will use the PAC spectroscopy to analyze the obtained In-doped Y_2O_3 samples both structurally and electronically.

The organization of this paper is as follows. In Section 2 we describe the sample preparation, and we briefly describe the PAC technique considering the purposes of our investigation. In Section 3 we present and discuss the obtained results. Finally, in Section 4 we give our conclusions.

2. Experimental details

2.1. Sample preparation

The starting materials were Y_2O_3 and In_2O_3 powders (99.99%, Aldrich) and other chemicals and reagents of analytical grade. In order to prepare 1% at. In-doped yttria, stoichiometric amounts of the oxides were dissolved in 12 ml of hydrochloric acid. The resulting solution was mixed with 3 ml of citric acid (1.7 M) and a few drops of ethylene glycol. The mixture was stirred and heated in open flask at about 400 K to promote polymerization, until dried, and then it was calcined for 12 h at 723 K to form the oxide. The resulting powder was pressed at about 60 kN into a pellet ½ inch diameter and thermally treated again for 12 h at 1473 K. The resulting pellets were about 2 mm thickness (we called this sample *PSGdoped*). A "pure" (undoped) Y_2O_3 sample was also prepared by the PSG method, following the same procedure as before but without including the In_2O_3 powder (*PSGpure*). After preparation, these pellets were characterized by XRD, and micro-Raman and EIS spectroscopies.

In order to compare the results obtained from these samples processed by the PSG method, we also prepared a reference pellet from the commercial Y_2O_3 powder, following the same thermal treatment than that mentioned above for the sol-gel powder pellet (*COMpure*).

On the other hand, to study the doped yttria by PAC spectroscopy we prepared three ^{111}In-doped Y_2O_3 samples. To this purpose, we repeated the PSG process described above to synthesize Y_2O_3 (PSGpure case), but adding about 4 μl of $^{111}InCl_3$ during the polymerization stage (activity below 100 μCi). By this way we obtained a radioactive pellet, called *PSGpoly*. The other two PAC samples were prepared by thermal diffusion, by dropping the same amount of $^{111}InCl_3$ as before on the Y_2O_3 pellets PSGpure and COMpure. In each case, the diffusion process was promoted by a thermal treatment in air of 1 h at 525 K followed by 12 h at 1473 K. The resulting radioactive samples were called *PSGthermal* and *COMthermal,* respectively.

2.2. Instrumentation

The resulting non-radioactive samples PSGpure, PSGdoped, and COMpure were characterized at room temperature by XRD (Rigaku Ultima IV, Cu Kα radiation), micro-Raman spectroscopy (WITec Alpha300RA, λ = 532 nm), and EIS spectroscopy (Gamry Inst. Ref. 3000).

The PAC measurements were performed on the radioactive samples PSGpoly, PSGthermal, and COM thermal, using the equipment described in Ref. [36]. The corresponding spectra were measured at different temperatures T in the range room temperature - 923 K.

2.3. The PAC spectroscopy

The PAC technique consists in the determination of the perturbation generated by extra-nuclear fields on the correlation between the emission directions of two successive γ radiations (γ_1 and γ_2) emitted during the decay of a radioactive probe-nucleus. The studied perturbation occurs during the lifetime of the intermediate state of the γ_1-γ_2 cascade. Using PAC, the EFG at a probe-nucleus can be determined through its interaction with the nuclear quadrupole moment Q [37].

The measured spin-rotation curve or $R(t)$ spectrum can be written as $R(t) \approx A_{22}G_{22}(t)$, where A_{22} is the experimental anisotropy of the γ_1-γ_2 cascade and $G_{22}(t)$ is the perturbation factor.

The PAC experiments presented in this paper were performed using the 171–245 keV γ_1-γ_2 cascade of ^{111}Cd, produced after the electron-capture (EC) nuclear decay of the parent nuclide ^{111}In, which has a half-life of 2.8 days. As mentioned above, for ^{111}In(→^{111}Cd)-doped yttria it is expected the presence of time-dependent ("dynamic") hyperfine interactions due to the observation of the electronic relaxation of the ^{111}Cd probe atom following the EC decay of ^{111}In. Almost all the electron holes produced by Auger processes following the EC diffuse in the valence band before the time-window of the PAC measurement but, depending on the electric character (conducting or insulating) of the host, some of them may be trapped close to the ^{111}Cd atom. Fast transitions among different ionization charge states of the Cd impurity will produce fluctuating EFGs giving rise to a time-dependent interaction. Therefore, to analyze each contribution to the PAC spectrum we considered the *effective* time-dependent perturbation factor [34]:

$$G_{22}(t) = [f_d e^{-\lambda t} + (1 - f_d)]G^s_{22}(t) \quad (1)$$

where the parameter f_d weights the dynamic interaction, *i.e.* the fraction of probe-nuclei that senses always a fluctuating EFG, and λ is the effective relaxation constant of the dynamic interaction [34,38]. The terms between square brackets modulate the "static" perturbation factor $G_{22}^s(t)$, which for the case under consideration (nuclear-electric-quadrupole interactions in polycrystalline samples and spin $I = 5/2+$ of the sensitive level of the ^{111}Cd probe-nucleus) takes the form [34].

$$G^s_{22}(t) = S_{20} + \sum_{n=1}^{3} S_{2n}(\eta)\cos(\omega_n(\eta)t)e^{-(\delta\omega_n t)} \quad (2)$$

where the coefficients S_{2n} and the interaction frequencies ω_n are known functions of the asymmetry parameter $\eta = (V_{xx} - V_{yy})/V_{zz}$, with V_{ii} the principal EFG tensor components ordered according to the convention $|V_{xx}| < |V_{yy}| < |V_{zz}|$. The ω_n frequencies are proportional to the nuclear quadrupole frequency $\omega_Q = eQV_{zz}/40\hbar$. Finally, δ stands for the half-width at half-maximum of the frequency distribution function around ω_n, which takes into account slightly different environments (and hence, EFGs) around a given probe site. In the scenario proposed by eq. (1), $(1\text{-}f_d)$ is the fraction of probes that senses always a "static" EFG

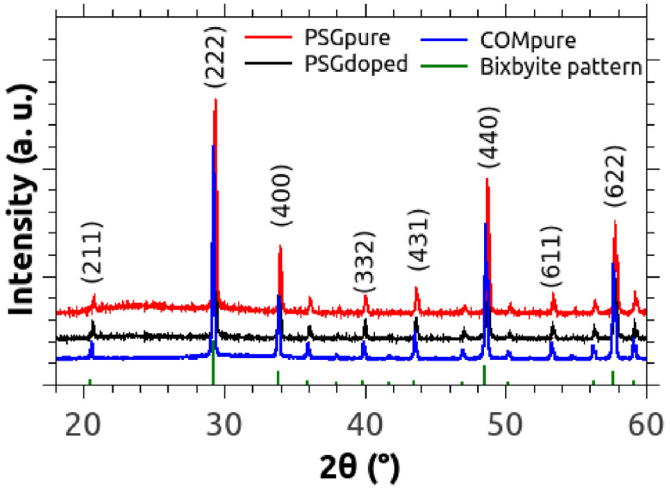

Fig. 1. XRD diffraction patterns for the different samples, and expected peaks for the yttria bixbyite structure.

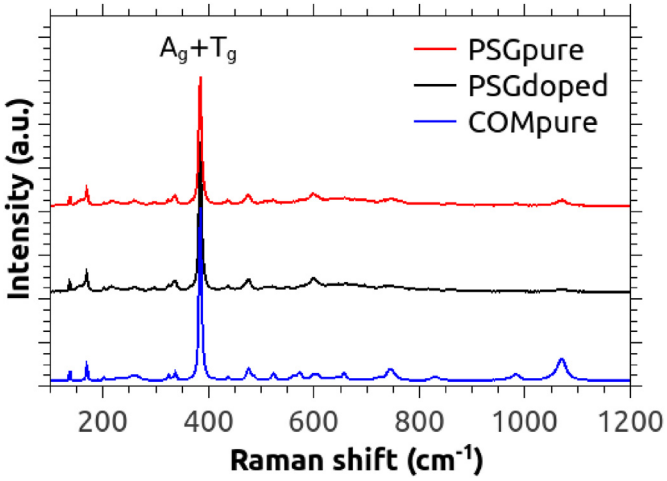

Fig. 2. Raman spectra for the different samples.

related with the static perturbation factor of eq. (2).

3. Results and discussion

3.1. X-ray diffraction

In Fig. 1 we present the XRD patterns corresponding to the PSGpure, PSGdoped, and COMpure samples. These patterns confirm the presence of the cubic bixbyite structure (space group Ia3) in the three samples as a single phase. In each case, in order to obtain the lattice parameter a and the crystalline size domain D we performed a Rietveld refinement analysis [39]. For the sample PSGpure we determined a = 10.6054 (5) Å and D = 145 (3) nm, for PSGdoped a = 10.6066 (4) Å and D = 146 (2) nm, whereas for COMpure a = 10.6067 (5) Å and D = 167 (4) nm. As can be seen, the very small differences between these lattice parameter values determined by Rietveld refinement are consistent with the slightly shifts of the XRD pattern observed in Fig. 1: higher a produces an XRD pattern shifted to smaller angles. In all these cases the D values are near below the limit of application of the refinement method due to the instrumental peak width, so they could be possibly slightly underestimated. Nevertheless, our results show that the PSG method successfully synthesize the oxide, with the same crystal structure than the commercial sample. On the other hand, although the presence of 1% In dopant in the host Y_2O_3 structure could not be evidenced by means of XRD analysis, the absence of other crystalline impurities suggests that including a small amount of In_2O_3 as starting material does not produce any significant change at this scale. Finally, the obtained lattice parameter values are within the range found in the literature for several different yttria samples at similar conditions (in the range 10.598–10.616 Å [40–44]).

3.2. Micro-Raman spectroscopy

The room temperature non-resonant Raman spectra are presented in Fig. 2. At first sight, the spectra for the three samples have similar features: a primary strong band at 390 cm^{-1} followed by many secondary peaks with intensities of 5% or below compared to that of the primary band. A closer look to the spectra reveals that the two samples processed by the PSG method (PSGpure and PSGdoped) have practically the same spectra, while the spectrum corresponding the COMpure presents sharper secondary peaks, especially for the high frequency modes (above 500 cm^{-1}). We used confocal Raman mapping to analyze the microscale spatial distribution of such modes. As example, in Fig. 3 we present for the PSGpure and COMpure samples the 2D Raman images generated by selecting the 390 and 1070 cm^{-1} peaks, as representatives of the different spectral regions. By performing this analysis, we checked that PSG samples exhibit a fine-grained, homogeneous microstructure, and confirmed that no segregated phase is observed.

Regarding the observed modes, although for the space group of the bixbyite structure there are expected 22 Raman active modes, $4A_g + 4E_g + 14T_g$, in previous experimental investigations a smaller number of peaks have been observed in the Raman spectra [45,46]. In this sense, different calculation methods support the assignment of the strong band at 390 cm^{-1} to $A_g + T_g$ modes and the high frequency Raman peaks to oxygen displacement modes [45,47–49]. In our case, the measured spectra presented in Fig. 2 are in good agreement with those previous studies and confirm that the samples have the same overall structural properties. In particular, we found that the PSGdoped sample has practically the same spectrum than the PSGpure one, which suggests that through the PSG process In dopants enter into the bixbyite host lattice without producing detectable changes to the crystalline structure.

3.3. Electrochemical impedance spectroscopy

Impedance spectra in the range 50 Hz-1 MHz were taken for the resulting pellets using stainless steel electrodes and DC bias voltages between 1 and 8 V. In Fig. 4 we present the Nyquist plots, expressed as the imaginary impedance ($-Z_{imag}$) as a function of real impedance (Z_{real}), measured for DC bias of 5 V as a representative example of the obtained results. As can be seen, for the three samples we obtained a fraction of the semicircle-like branch. In Fig. 4a it can be best appreciated the differences at low frequencies, for higher values of Z_{real}, where the PSGpure and PSGdoped samples have a more open arc in the Nyquist plot compared to that of the COMpure sample. On the other hand, Fig. 4b shows that at high frequencies, for lower values of Z_{real}, this situation is inverted, and the COMpure sample has the arc with the highest radius. Similar features are observed for all the considered DC bias voltages.

We analyzed these impedance data by fitting to the equivalent electrical circuit showed in the inset of Fig. 4a, which consists of two R-CPE circuits connected in series, each of which are composed by a resistance connected in parallel to a constant phase element (CPE). Each CPE element represents a non-ideal capacitor, and its impedance can be expressed as:

$$Z_{\mathrm{CPE}} = [(j\omega)^{\alpha} Y_0]^{-1},$$

where Y_0 is the capacitance and a an exponent that equals unity when the element behaves as an ideal capacitor. In the proposed model, one parallel R-CPE pair stands for the grain interiors contribution to the

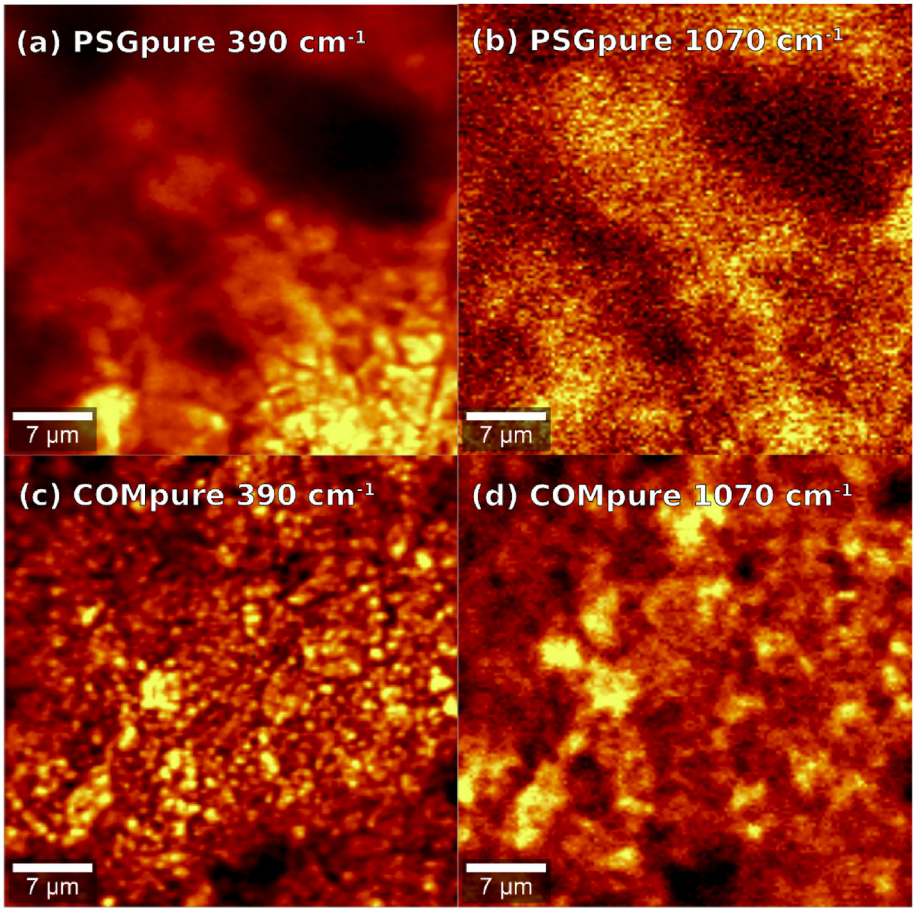

Fig. 3. 2D Raman mapping for the 390 and 1070 cm^{-1} peaks in the (a, b) PSGpure and the (c, d) COMpure samples.

total impedance, whereas the other pair stands for the grain boundaries contribution. We define R_{gi} and R_{gb} as the resistance for each contribution, respectively, from which we can determine the corresponding resistivities ρ by considering the pellet diameter and thickness. In this respect, in a typical Nyquist plot, the grain interior is associated with the high frequency region (near the Nyquist plot origin, Fig. 4b), while the electrical transport through the grain boundaries is related to the lower frequencies (the open arc part and beyond, Fig. 4a). These assignments are in agreement with previous works [15,50–52]. In the present case, the inversion of impedance arc behavior from lower (Fig. 4a) to higher frequency region (Fig. 4b) is indicating that PSG samples have lower grain interior resistivity but higher grain boundary resistivity than COM samples. This could be associated to the enhanced homogeneity of grain interiors but lower crystallinity of PSG samples compared to COM samples. So, from the least-squares fits of the model to the impedance data (solid lines in Fig. 4a) we determined the different contributions to the total impedance. In Fig. 5 we plot the ρ results (in log scale) against the DC bias voltage. According to literature, typical values of the resistivities in yttria samples ranges between 10^7 and 10^9 Ωmm, and broadly depend on the sample structure, composition, particle size and impurities [14,15,50]. So, our results are in a general agreement with these previous measurements. As can be seen in Fig. 5, for the PSG processed samples the grain interior contribution (ρ_{gi}) is about two orders of magnitude lower than the grain boundary contribution (ρ_{gb}), being each contribution in the same order for both samples (PSGpure and PSGdoped). In particular, we found that ρ_{gi} for

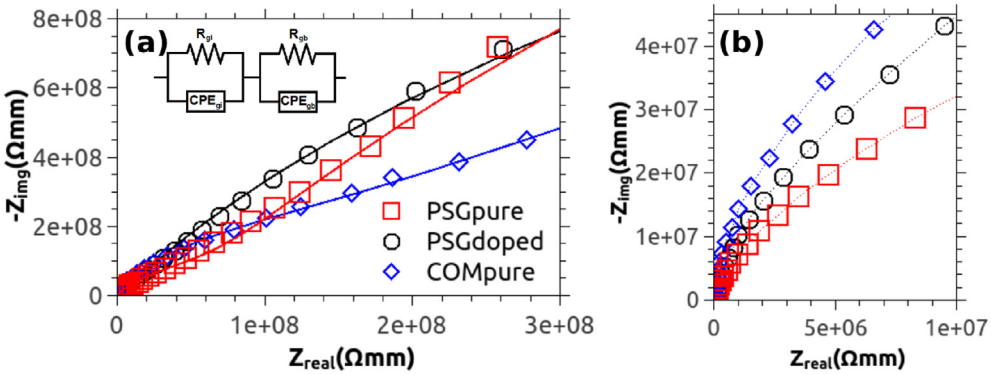

Fig. 4. (a) Nyquist plots data for impedance curves collected for the different samples with DC bias = 5 V. The solid lines are the least-squares fits of the proposed equivalent circuit shown in the inset. (b) Zoom of the plot for the low-impedance regime at high frequencies.

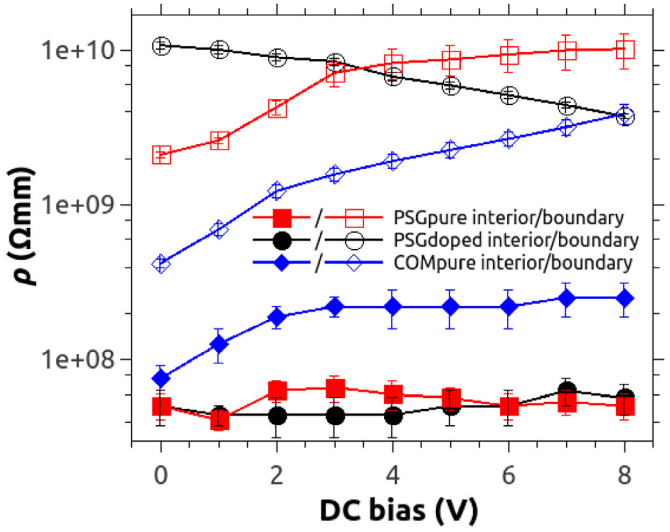

Fig. 5. Resistivity (ρ) values for the different samples at their grain interiors (filled symbols) and grain boundaries (hollow symbols) as a function of the applied DC bias voltage.

these samples are practically the same, which means that In doping of the host structure does not affect the resistivity, but only for a slight decrease in ρ_{gb} with increasing DC voltage. On the other hand, for the COMpure sample the difference between ρ_{gi} and ρ_{gb} is lower (of one order of magnitude) compared to that of the PSG samples. Considering that all samples have nearly the same crystalline size domain, as observed by XRD, these obtained results for the resistivities suggest that it is the PSG process itself (and not the In doping or a grain size effect) which defines the differences in ρ values comparing to those of the COMpure sample. According to these results, the PSG samples have better conductivities at grain interiors than the pellet produced directly from commercial powder. Finally, from the fits we also determined the CPE parameters, with Y_0 values in the range 40–60x10^{-12} F^a, and the a exponent takes values in the range 0.9–1.

3.4. PAC spectroscopy

In Fig. 6 we present representative $R(t)$ spectra for the three radioactive ^{111}In-doped Y_2O_3 samples, measured at a temperature T in the range 273–973 K. As can be seen, for each sample the spectrum taken at room temperature presents a strong damping compared to that of higher temperatures, being this damping reversible with temperature. In particular, a close inspection of the COMthermal sample (Fig. 6c) shows a strong damping in the first 50 ns and a rather constant amplitude of the rest o the spectra. This behavior reflects the presence of time-dependent dynamic hyperfine interactions at the ^{111}Cd probe sites related with the EC decay after-effects [34,54–56]. On the other hand, we observe that while the PAC spectrum at 973K for the COMthermal sample still exhibits some degree of damping, the $R(t)$ is practically undampened for the PSGpoly and PSGthermal samples at this high temperature (see Fig. 6a and b). In order to quantitatively analyze such differences, we fitted the $R(t)$ spectra using the perturbation factor presented in Section 2.3. To this purpose, considering the obtained structural results and previous PAC measurements on doped bixbyites [21,53–56], we proposed two hyperfine interactions, called C and D, in a relation 3:1. These two hyperfine interactions are associated to the (^{111}In→)^{111}Cd probes located at substitutional defect-free cationic sites C and D of the cubic bixbyite structure, being the population ratio of such interactions in agreement with the relative abundance of the cationic sites in the bixbyite structure [32,40,56]. We found that these interactions are enough to account for the experimental spectra. In this sense, the solid lines in the PAC spectra of Fig. 6 are the best least-squares fits of eqs. (1) and (2) to the experimental data.

In Fig. 7 we show the fitted values for $|V_{zz}|$, η, f_d, and λ parameters as a function of T for the different samples and probe sites. We used $Q = 0.76$ (2) b [57] to obtain $|V_{zz}|$ from the nuclear quadrupole frequency ω_Q. At high temperatures ($T > 600$ K), for both interactions δ is below 5%, which means that the interactions are well defined and the static perturbation factor is nearly undampened. The main interaction C is characterized by a highly asymmetric EFG ($\eta > 0.6$), while for the second interaction D the EFG is axially symmetric ($\eta \approx 0$). These results are in agreement with the symmetry of the cationic sites in the bixbyite structure [40], and support the scenario of impurity probe atoms substitutionally located at such sites, as proposed above. Considering this interaction assignment, $|V_{zz}{}^C|$ and $|V_{zz}{}^D|$ are about 4.5 and 8.0 × 10^{21} Vm^{-2}, respectively. Regarding the dynamic interactions, at temperatures below 600 K the PAC spectra are strongly dampened. If we consider the main interaction C, we observe that the weight of the dynamic interaction f_d takes values in the range 0.8–1. Near 600 K this parameter becomes null for the PSGpoly and PSGthermal samples, whereas for COMthermal is still appreciable and about 0.6, even for higher temperatures than 600 K. On the other hand, we found that for the dynamic regime the relaxation constant λ is below 1 ns^{-1}. Similar results are observed for the f_d and λ parameters of the secondary interaction D. These parameters reflect the behavior of the PAC spectra with temperature described above for Fig. 6. In this sense, the f_d vs T curves for the PSG processed samples (PSGpoly and PSGthermal) show that the dynamic interactions are suppressed for temperatures above 600 K, while for the COMthermal sample the EC decay after-effects are observed even at the highest temperature. This result indicates that the PSG method produces a host structure where the electron availability detected through the probe's EC decay after-effects changes more significantly with T compared to the sample produced from commercial powder. This is in agreement with the EIS results, and suggests that the PSG process produces donor defects in the form of additional impurities, inhomogeneities, or deviations from the Y_2O_3 stoichiometry that influence the electronic behavior in a different way to that observed in the commercial sample. In particular, it promotes a higher electron availability near the probe nuclei with increasing temperature and, consequently, the effective time-dependent perturbation factor becomes static at T greater than 600 K. Note also that the response of the PAC spectra with T for PSGpoly and PSGthermal samples is practically the same, which suggests that the electron availability does not depend on when and how the ^{111}In probe is introduced into the host structure (i.e., during polymerization stage or at the end through thermal diffusion).

4. Discussion

The obtained results allow us to present a comprehensive study of the structural and electronic properties of the samples produced by the PSG process. Regarding the structural characterization, the experimental techniques considered in this work cover a wide range of scales, going from the crystallographic structure to the atomic local environments. In this sense, the XRD and Raman measurements showed that the PSG process produce nanocrystalline In-doped Y_2O_3 samples with the cubic bixbyite structure, and the Raman mapping showed that pellets are composed of a fine-grained homogeneous powder, as observed in previous studies by scanning electron microscopy [21]. Regarding the In impurity localization in the Y_2O_3 host structure, the XRD, Raman and PAC data suggested that impurities are substitutionally located at the sites C and D of the bixbyite structure. This assumption was unambiguously supported by the measured hyperfine parameters. Moreover, the PAC results showed that these sites are free of defects, as a consequence of the sensitivity of the EFG to detect both structural or electronic defects. In particular, the EFG values presented in Fig. 7 are practically the same to those previously reported for ^{111}In-implanted Y_2O_3 [53] and fit to the EFG systematics constructed considering the

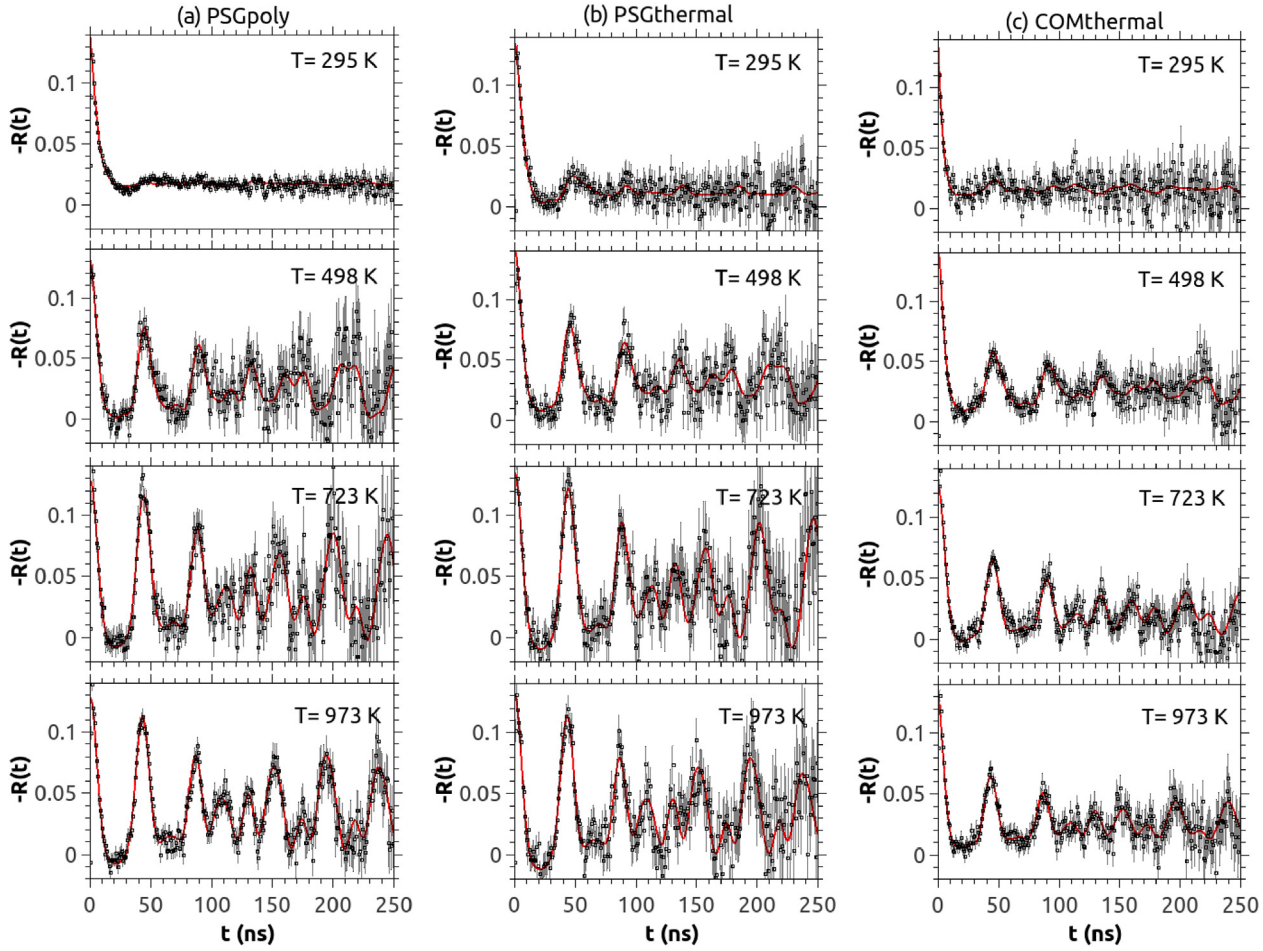

Fig. 6. PAC spectra taken at representative measuring temperatures T for the (a) PSGpoly, (b) PSGthermal, and (c) COMthermal samples.

^{111}Cd PAC measurements in other oxides isomorphous to Y_2O_3 [32]. Also, these values are in agreement with those recently predicted by first-principles calculations considering a system where the Cd impurities are located at the substitutional cationic sites of cubic yttria [58].

On the other hand, regarding the electronic properties, we found that for the PSG samples the presence of In impurity atoms in the Y_2O_3 structure does not produce significant changes in the EIS spectra. However, compared to the COMpure pellet, the PSG processing method produces yttria samples with differences in the impedance spectra, in both the pure and In-doped case. In particular, we found that the PSG samples have much better conductivities at grain interiors than the reference commercial pellet. These differences were confirmed with the analysis of the dynamic hyperfine interactions observed by PAC spectroscopy, using (^{111}In→)^{111}Cd as probe atom. In this sense, PAC spectroscopy showed that increasing temperature promotes a higher electron availability near probes in the PSG samples. We speculate that PSG process produces structural donor defects additional to the presence of In impurities. These defects could be related to the subtle differences between PSG samples and the commercial sample observed in the high frequency modes of their Raman spectra (see Fig. 2).

In summary, in this study we used PAC spectroscopy as a key complement to other experimental techniques to relate the subnanoscopic structure to the electronic properties of the yttria samples. Our results demonstrate that the PSG process can be used to produce yttria samples that are electronically different to commercial ones, a fact that should be considered to analyze the electronic response on samples produced by this process and other similar sol-gel methods for technological purposes.

5. Conclusions

We demonstrated that the PSG process successfully produces fine-grained nanocrystalline In-doped yttria powders. According to our data, the obtained samples crystallize in the cubic bixbyite structure and the In impurities are substitutionally located at the cationic sites. The EIS measurements showed that the PSG samples have better conductivities at grain interiors than the reference pellet produced from Y_2O_3 commercial powder, and that In doping in the PSG process does not significantly affect the resistivity. PAC spectroscopy in the ^{111}In(→^{111}Cd)-doped yttria samples supports these results. In particular, the study of the dynamic hyperfine interactions as a function of measuring temperature showed that, depending on the sample production method, there is a different response of the electron availability near the impurities. These results open a path toward understanding the structural and electronic properties that the sol-gel processing methods can provide, and should be considered in future research.

Declaration of competing interest

The authors declare that they have no known competing financial interests or personal relationships that could have appeared to influence the work reported in this paper.

Acknowledgments

We wish to acknowledge the Argentinian, Brazilian and Uruguayan funding institutions, Consejo Nacional de Investigaciones Científicas y Técnicas (CONICET, under grant no. PIP0803), Conselho Nacional de

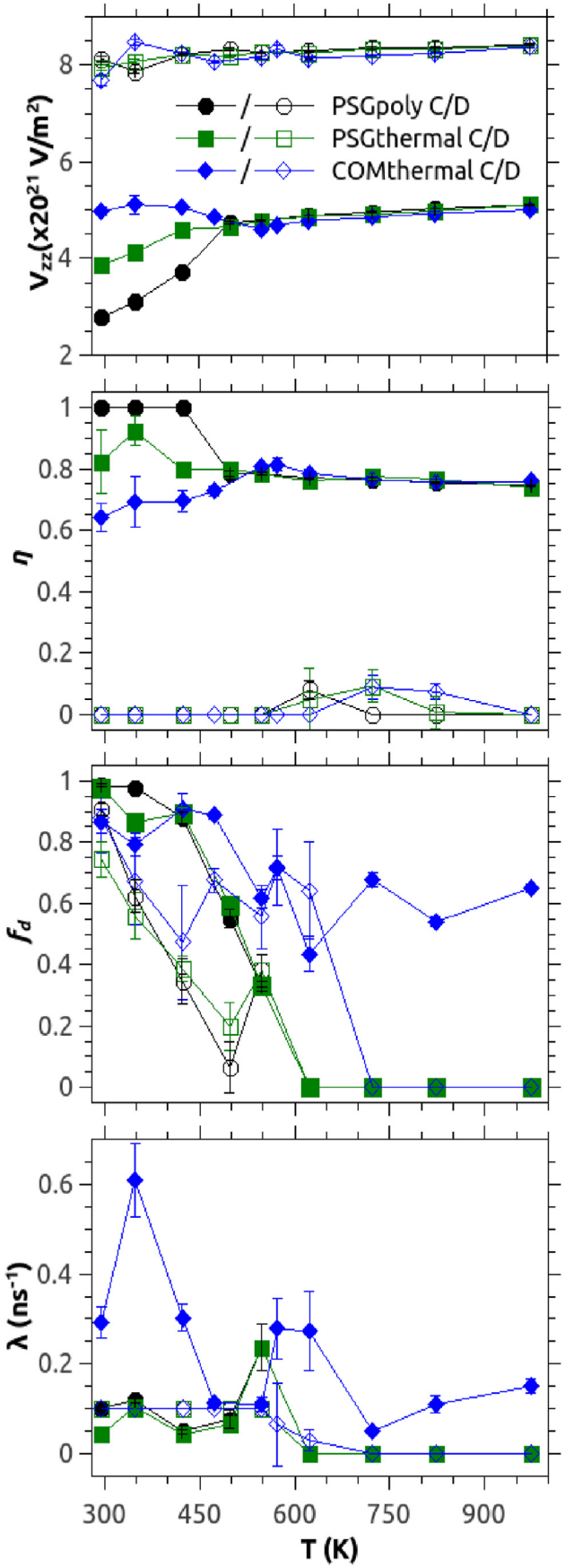

Fig. 7. Temperature dependence of the hyperfine parameters for the different samples and probe sites C and D.

Desenvolvimento Científico e Tecnológico (CNPq, grant no. 305046/2013-6), Fundação de Amparo a Pesquisa do Estado de São Paulo (FAPESP, grant no. 2014/14001-1), and Agencia Nacional de Investigación e Innovación (ANII, grant no. PD_NAC_2015_1_108453). D. Richard and M. Rentería are members of CONICET, Argentina. M. Romero and R. Faccio acknowledge PEDECIBA, ANII and CSIC, Uruguayan Institutions.

References

[1] M.G. Ivanov, U. Kynast, M. Leznina, Eu^{3+} doped yttrium oxide nano-luminophores from laser synthesis, J. Lumin. 169 (2016) 744–748, https://doi.org/10.1016/j.jlumin.2015.05.036.

[2] R. Shoja Razavi, M. Ahsanzadeh-Vadeqani, M. Barekat, M. Naderi, S.H. Hashemi, A. Kumar Mishra, Effect of sintering temperature on microstructural and optical properties of transparent yttria ceramics fabricated by spark plasma sintering, Ceram. Int. 42 (2016) 7819–7823, https://doi.org/10.1016/j.ceramint.2016.02.013.

[3] M. Ghaderi, R. Shoja Razavi, M.R. Loghman-Estarki, S. Ghorbani, Spark plasma sintering of transparent Y_2O_3 ceramic using hydrothermal synthesized nano-powders, Ceram. Int. 42 (2016) 14403–14410, https://doi.org/10.1016/j.ceramint.2016.06.022.

[4] K.C. Camargo, R.R. Pereira, L.F. dos Santos, S.R. de Oliveira, R.R. Gonçalves, L.de S. Menezes, Continuous wave near-infrared phonon-assisted upconversion in single Nd^{3+}-doped yttria nanoparticles, J. Lumin. 192 (2017) 963–968, https://doi.org/10.1016/j.jlumin.2017.08.031.

[5] Q. Chen, L. Luo, L. Wang, T. Xie, S. Dai, Y. Yang, Y. Li, M. Yuan, Enhanced electrochemical properties of Y_2O_3-coated-(lithium-manganese)-rich layered oxides as cathode materials for use in lithium-ion batteries, J. Alloys Compd. 735 (2018) 1778–1786, https://doi.org/10.1016/j.jallcom.2017.11.362.

[6] J. Li, O. Yin, L. Zhao, Z. Wang, B. Dong, L. Wan, S. Wang, Enhancing the photoelectric conversion efficiency of dye-sensitized solar cell using the upconversion luminescence materials Y_2O_3 :Er^{3+} nanorods doped TiO_2 photoanode, Mater. Lett. 227 (2018) 209–212, https://doi.org/10.1016/j.matlet.2018.05.057.

[7] R.S. Yadav, S.B. Rai, Concentration and wavelength dependent frequency down-shifting photoluminescence from a Tb^{3+} doped yttria nano-phosphor: a photochromic phosphor, J. Phys. Chem. Solid. 114 (2018) 179–186, https://doi.org/10.1016/j.jpcs.2017.11.025.

[8] S. Dai, M. Yuan, L. Wang, L. Luo, T. Xie, Q. Chen, T. Xie, Y. Li, Y. Yang, Ultrathin-Y_2O_3-coated $LiNi_{0.8}Co_{0.1}Mn_{0.1}O_2$ as cathode materials for Li-ion batteries: synthesis, performance and reversibility, Ceram. Int. 45 (2019) 674–680, https://doi.org/10.1016/j.ceramint.2018.09.227.

[9] L. Lin, S. Starostin, X. Ma, S. Li, S.A. Khan, V. Hessel, Facile synthesis of lanthanide doped yttria nanophosphors by a simple microplasma-assisted process, React. Chem. Eng. 4 (2019) 891–898, https://doi.org/10.1039/c8re00357b.

[10] R.V. Mangalaraja, J. Mouzon, P. Hedström, I. Kero, K.V.S. Ramam, C.P. Camurri, M. Odén, Combustion synthesis of Y2O3 and Yb-Y2O3, J. Mater. Process. Technol. 208 (2008) 415–422, https://doi.org/10.1016/j.jmatprotec.2008.01.023.

[11] A. Mohammadi, Y. Ganjkhanlou, A.B. Moghaddam, M. Kazemzad, F.A. Hessari, R. Dinarvand, Synthesis of nanocrystalline Y_2O_3:Eu phosphor through different chemical methods: studies on the chromaticity dependence and phase conversion, Micro & Nano Lett. 7 (2012) 515–518, https://doi.org/10.1049/mnl.2012.0153.

[12] V. De la Luz, M. Prades, H. Beltrán, E. Cordoncillo, Environmental-friendly yellow pigment based on Tb and M (M= Ca or Ba) co-doped Y_2O_3, J. Eur. Ceram. Soc. 33 (2013) 3359–3368, https://doi.org/10.1016/j.jeurceramsoc.2013.05.021.

[13] T.C. de Oliveira, M.S. Silva, L.M. de Jesus, D. Vieira Sampaio, J.C. Alves dos Santos, N.R. da Silva Souza, R.S. da Silva, Laser sintering and radioluminescence emission of pure and doped Y_2O_3 ceramics, Ceram. Int. 40 (2014) 16209–16212, https://doi.org/10.1016/j.ceramint.2014.07.056.

[14] A. Jyotsana, G.S. Maurya, A.K. Srivastava, A.K. Rai, B.K. Ghosh, Synthesis and electrical properties of Y_2O_3: Dy^{3+} & Eu^{3+} nanoparticles, Appl. Phys. A 117 (2014) 1269–1274, https://doi.org/10.1007/s00339-014-8516-y.

[15] G. Bhavani, S. Ganesan, S. Selvasekarapandian, S. Monisha, M. Premalatha, Synthesis and electrical characterisation of zinc-doped yttrium oxide, Ionics 22 (2015) 581–592, https://doi.org/10.1007/s11581-015-1565-1.

[16] D.Y. Medina Velazquez, L.A. Hernández Soto, Á. de J. Morales Ramirez, S. Carmona-Téllez, E. Garfias-Garcia, C. Falcony, A. García Murillo, White luminescence of bismuth and samarium codoped Y_2O_3 phosphors, Ceram. Int. 41 (2015) 8481–8487, https://doi.org/10.1016/j.ceramint.2015.03.054.

[17] N.J. Shivaramu, B.N. Lakshminarasappa, K.R. Nagabhushana, F. Singh, Thermoluminescence of sol-gel derived Y_2O_3:Nd^{3+} nanophosphor exposed to 100MeV Si^{8+} ions and gamma rays, J. Alloys Compd. 637 (2015) 564–573, https://doi.org/10.1016/j.jallcom.2015.02.218.

[18] E. Delon, F. Ansart, S. Duluard, J.P. Bonino, A. Malié, A. Joulia, P. Gomez, Synthesis of yttria by aqueous sol-gel route to develop anti-CMAS coatings for the protection of EBPVD thermal barriers, Ceram. Int. 42 (2016) 13704–13714, https://doi.org/10.1016/j.ceramint.2016.05.169.

[19] M. Hajizadeh-Oghaz, R.S. Razavi, M. Barekat, M. Naderi, S. Malekzadeh, M. Rezazadeh, Synthesis and characterization of Y_2O_3 nanoparticles by sol-gel process for transparent ceramics applications, J. Sol. Gel Sci. Technol. 78 (2016) 682–691, https://doi.org/10.1007/s10971-016-3986-3.

[20] N.J. Shivaramu, K.R. Nagabhushana, B.N. Lakshminarasappa, F. Singh, Ion beam induced luminescence studies of sol gel derived Y_2O_3 :Dy^{3+} nanophosphors, J.

Lumin. 169 (2016) 627–634, https://doi.org/10.1016/j.jlumin.2015.07.054.
[21] D. Richard, M. Rentería, A.W. Carbonari, Substitutional Ta-doping in Y_2O_3 semiconductor by sol-gel synthesis: experimental and theoretical studies, Semicond. Sci. Technol. 32 (2017) 085010, , https://doi.org/10.1088/1361-6641/aa7a74.
[22] M. de Oliveira Krauser, H.H. de Souza Oliveira, M.A. Cebim, M.R. Davolos, Relationship between scintillation properties and crystallite sizes in Y_2O_3:Eu^{3+}, J. Lumin. 203 (2018) 100–104, https://doi.org/10.1016/j.jlumin.2018.06.038.
[23] I.E. Kolesnikov, D.V. Mamonova, E. Lähderanta, E. Yu Kolesnikov, A.V. Kurochkin, M.D. Mikhailov, Synthesis and characterization of Y_2O_3:Nd^{3+} nanocrystalline powders and ceramics, Opt. Mater. 75 (2018) 680–685, https://doi.org/10.1016/j.optmat.2017.11.032.
[24] K. Rubešová, T. Thoř, V. Jakeš, D. Mikolášová, J. Maixner, O. Jankovský, J. Cajzl, L. Nádherný, A. Beitlerová, M. Nikl, Lanthanide-doped Y_2O_3 - the photoluminescent and radioluminescent properties of sol-gel prepared samples, Ceramics-Silikáty 62 (2018) 411–417, https://doi.org/10.13168/cs.2018.0038.
[25] L. Klein, M. Aparicio, A. Jitianu, Handbook of Sol-Gel Science and Technology, Springer, 2018, https://doi.org/10.1007/978-3-319-32101-1.
[26] S. Esposito, "Traditional" sol-gel chemistry as a powerful tool for the preparation of supported metal and metal oxide catalysts, Materials 12 (2019) 668, https://doi.org/10.3390/ma12040668.
[27] J. Lin, M. Yu, C. Lin, X. Liu, Multiform oxide optical materials via the versatile Pechini-type sol-gel process: synthesis and characteristics, J. Phys. Chem. C 111 (2007) 5835–5845, https://doi.org/10.1021/jp070062c.
[28] L. Dimesso, Pechini processes: an alternate approach of the sol-gel method, preparation, properties, and applications, in: L. Klein, et al. (Ed.), Handbook of Sol-Gel Science and Technology, Springer, 2018, , https://doi.org/10.1007/978-3-319-32101-1_123.
[29] A. Dupont, C. Parent, B. Le Garrec, J.M. Heintz, Size and morphology control of Y_2O_3 nanopowders via a sol-gel route, J. Solid State Chem. 171 (2003) 152–160, https://doi.org/10.1016/S0022-4596(02)00202-5.
[30] A.M. Pires, O.A. Serra, M.R. Davolos, Morphological and luminescent studies on nanosized Er, Yb-yttrium oxide up-converter prepared from different precursors, J. Lumin. 113 (2005) 174–182, https://doi.org/10.1016/j.jlumin.2004.09.122.
[31] M. Uhrmacher, Application of perturbed angular correlations to oxides, Physica B 389 (2007) 58–66, https://doi.org/10.1016/j.physb.2006.07.025.
[32] A.F. Pasquevich, M. Rentería, Impurity centers in oxides investigated by γ–γ perturbed angular correlation spectroscopy and ab initio calculations defect, Defect Diffusion Forum 311 (2011) 62–104 https://doi.org/10.4028/www.scientific.net/DDF.311.62.
[33] E.L. Muñoz, PhD Thesis: Estudio experimental y de primeros principios de interacciones hiperfinas dinámicas en óxidos semiconductores dopados con impurezas, Universidad Nacional de La Plata, 978-950-34-0784-4, 2011.
[34] G.N. Darriba, E.L. Muñoz, A.W. Carbonari, M. Rentería, Experimental TDPAC and theoretical DFT study of structural, electronic, and hyperfine properties in (^{111}In→)^{111}Cd-doped SnO_2 semiconductor: ab initio modeling of the electron-capture-decay after-effects phenomenon, J. Phys. Chem. C 122 (2018) 17423–17436, https://doi.org/10.1021/acs.jpcc.8b03724.
[35] A. Lohstroh, M. Uhrmacher, P.J. Wilbrandt, H. Wulff, L. Ziegeler, K.P. Lieb, Electronic relaxation in indium oxide films studied with perturbed angular correlations, Hyperfine Interact. 159 (2004) 35–42, https://doi.org/10.1007/s10751-005-9078-3.
[36] R. Valentini, R. Vianden, PAC studies with LSO scintillation crystals, Nucl. Instrum. Methods 623 (2010) 1002–1008, https://doi.org/10.1016/j.nima.2010.07.084.
[37] G. Schatz, A. Weidinger, Nuclear Condensed Matter Physics: Nuclear Methods and Applications, Wiley, Chichester, 1996.
[38] U. Bäverstam, R. Othaz, N. De Sousa, B. Ringström, After-effects in the decay of ^{57}As and ^{197m}Hg, Nucl. Phys. 186 (1972) 500–512.
[39] A.C. Larson, R.B. Von Dreele, General structure analysis system (GSAS), Los Alamos Natl Lab Report LAUR 86 (2004) 748.
[40] N. Maslen, V.A. Streltsov, N. Ishizawa, A synchrotron x-ray study of the electron density in C-type rare earth oxides, Acta Crystallogr. B 52 (1996) 414–422, https://doi.org/10.1107/S0108768195013371.
[41] B. Allieri, L.E. Depero, A. Marino, L. Sangaletti, L. Caporaso, A. Speghini, M. Bettinelli, Growth and microstructural analysis of nanosized Y_2O_3 doped with rare-earths, Mater. Chem. Phys. 66 (2000) 164–171, https://doi.org/10.1016/S0254-0584(00)00325-4.
[42] F.F. Ferreira, E. Granado, W. Carvalho Jr., S.W. Kycia, D. Bruno, R. Droppa Jr., X-ray powder diffraction beamline at D10B of LNLS: application to the Ba_2FeReO_6 double perovskite, J. Synchrotron Radiat. 13 (2006) 46–53, https://doi.org/10.1107/S0909049505039208.
[43] L. Wang, Y. Pan, Y. Ding, W. Yang, W.L. Mao, S.V. Sinogeikin, Y. Meng, G. Shen, H. Mao, High-pressure induced phase transitions of Y_2O_3 and Y_2O_3:Eu^{3+}, Appl. Phys. Lett. 94 (2009) 061921, , https://doi.org/10.1063/1.3082082.
[44] S. Jiang, J. Liu, X.-D. Li, Y.-C. Li, S.-M. He, J.-C. Zhang, High-pressure phase transitions of cubic Y_2O_3 under high pressures by in-situ synchrotron x-ray diffraction, Chin. Phys. Lett. 36 (2019) 046103, , https://doi.org/10.1088/0256-307X/36/4/046103.
[45] M.V. Abrashev, N.D. Todorov, J. Geshev, Raman spectra of R_2O_3 (R- rare earth) sesquioxides with C-type bixbyite crystal structure: a comparative study, J. Appl. Phys. 166 (2014) 103508, https://doi.org/10.1063/1.4894775.
[46] N. Dilawar Sharma, J. Singh, A. Vijay, K. Samanta, S. Dogra, A.K. Bandyopadhyay, Pressure-induced structural transition trends in nanocrystalline rare-earth sesquioxides: a Raman investigation, J. Phys. Chem. C 120 (2016) 11679–11689, https://doi.org/10.1021/acs.jpcc.6b02104.
[47] Y. Repelin, C. Proust, E. Husson, J.M. Beny, Vibrational spectroscopy of the C-form of yttrium sesquioxide, J. Solid State Chem. 118 (1995) 163–169, https://doi.org/10.1006/jssc.1995.1326.
[48] J.Q. Xu, S.J. Xiong, X.L. Wu, T.H. Li, J.C. Shen, P.K. Chu, Investigation of activated oxygen molecules on the surface of Y_2O_3 nanocrystals by Raman scattering, J. Appl. Phys. 114 (2013) 093512, , https://doi.org/10.1063/1.4820465.
[49] T. Ogawa, N. Otani, T. Yokoi, C.A.J. Fisher, A. Kuwabara, H. Moriwake, M. Yoshiya, S. Kitaoka, M. Takata, Density functional study of phase stabilities and Raman spectra of Yb_2O_3, Yb_2SiO_5 and $Yb_2Si_2O_7$ under pressure, Phys. Chem. Chem. Phys. 20 (2018) 16518–16527, https://doi.org/10.1039/C8CP02497A.
[50] C.A. Witt, Thermionic insulator testing (AC impedance spectroscopy), Proceedings of the 24th Intersociety Energy Conversion Engineering Conference, 1989, https://doi.org/10.1109/iecec.1989.74400.
[51] D. Mombrú, M. Romero, R. Faccio, A.W. Mombrú, Raman and impedance spectroscopy under applied dc bias insights on the electrical transport for donor: acceptor nanocomposites based on poly(vinyl carbazole) and TiO_2 quantum dots, J. Phys. Chem. C 121 (2017) 23383–23391, https://doi.org/10.1021/acs.jpcc.7b08400.
[52] D. Richard, M. Romero, R. Faccio, Experimental and theoretical study on the structural, electrical and optical properties of tantalum-doped ZnO nanoparticles prepared via sol-gel acetate route, Ceram. Int. 44 (2018) 703–711, https://doi.org/10.1016/j.ceramint.2017.09.232.
[53] A. Bartos, K.P. Lieb, A.F. Pasquevich, M. Uhrmacher, The ISOLDE collaboration, Scaling of the electric field gradient of ^{111}Cd impurities in the bixbyite oxides of Y, Sc, Dy and Yb, Phys. Lett. A 157 (1991) 513–518, https://doi.org/10.1016/0375-9601(91)91029-D.
[54] S. Habenicht, D. Lupascu, M. Uhrmacher, L. Ziegeler, K.P. Lieb, ISOLDE Collaboration, PAC-studies of Sn-doped In_2O_3: electronic defect relaxation following the ^{111}In(EC) ^{111}Cd-decay, Z. Phys. B 101 (1996) 187–196, https://doi.org/10.1007/s002570050199.
[55] E.L. Muñoz, D. Richard, A.W. Carbonari, L.A. Errico, M. Rentería, PAC study of dynamic hyperfine interactions at ^{111}In-doped Sc_2O_3 semiconductor and comparison with ab initio calculations, Hyperfine Interact. 197 (2010) 199–205, https://doi.org/10.1007/s10751-010-0207-2.
[56] D. Richard, G.N. Darriba, E.L. Muñoz, L.A. Errico, P.D. Eversheim, M. Rentería, Experimental and first-principles theoretical study of structural and electronic properties in tantalum-doped In_2O_3 semiconductor: finding a definitive hyperfine interaction assignment, J. Phys. Chem. C 120 (2016) 5640–5650, https://doi.org/10.1021/acs.jpcc.5b11155.
[57] L. Errico, K. Lejaeghere, J. Runco, S.N. Mishra, M. Rentería, S. Cottenier, Precision of electric-field gradient predictions by Density Functional Theory and implications for the nuclear quadrupole moment and its error bar of the ^{111}Cd 245 keV 5/2+ level, J. Phys. Chem. C 120 (2016) 23111–23120, https://doi.org/10.1021/acs.jpcc.6b06127.
[58] D. Richard, A.V. Gil Rebaza, The GIPAW approach for the study of local structures and the electric field gradients at Cd and Ta impurity sites. Application to doped yttria ceramics, Comput. Mater. Sci. 171 (2020) 109224, https://doi.org/10.1016/j.commatsci.2019.109224.